Plasma rings in laser-induced plasma

Video URL: goo.gl/MqobD0

Author :   S. Zwaan
Student ID :   1255010
Supervisor :   D.Bouwmeester
                                  C. Smiet
2nd corrector :   S.J. van der Molen

Leiden, The Netherlands, July 8, 2016

Plasma rings in laser-induced plasma

S. Zwaan

Huygens-Kamerlingh Onnes Laboratory, Leiden University
P.O. Box 9500, 2300 RA Leiden, The Netherlands

July 8, 2016

Abstract

Recently it was observed that laser-induced breakdown creates macroscopic rings of plasma. These rings are of interest because they can be used to construct inherently stable magnetized plasma structures. The goal is to form a better understanding of the processes within and properties of these plasma rings. We study the different stages in the time-evolution of the plasma using an intensified CCD with nanosecond resolution exposure time. Furthermore, the spectrum of the emitted light is studied and through Boltzmann analysis the temperature is derived.

Keywords: plasma, Helium, atmospheric pressure, laser-induced breakdown, spectrum

Contents

Chapter 1

Introduction

Plasmas are created when the atoms in a gas become ionized. Plasma exist in many forms, from the vacuum of outer space to the dense core of our sun. Plasmas are also used in nuclear fusion reactors like Tokamaks, which are unfortunately not yet efficient enough to produce energy. Gaining a better understanding of plasmas may bring profitable nuclear fusion one step closer.

Gases can be described by fluid dynamics, but for plasmas this is not sufficient. The ionization of the atoms creates free negatively charged electrons, leaving positively charged ions behind. Because of the freely moving charged particles, electromagnetic forces play a big part in the dynamics of a plasma. To fully describe plasmas, the theories of fluid dynamics have been combined with Maxwell's equations to form Magnetohydrodynamics (MHD).

Simulations using MHD have been done starting with linked magnetic field lines [8]. As the plasma evolves in time the linking of the field-lines remains approximately conserved. The field-lines form a ring-structure which stabilizes the plasma through a balance of the Lorentz-force and hydro-static pressure.

To investigate whether such configurations can be created in the lab, a set-up has been built which creates plasmas through laser-induced breakdown in Helium at atmospheric pressure. Interestingly, these plasmas spontaneously form a ring structure. Experiments have been done on the effect of using pre-ionization on the Helium before the laser-induced breakdown [1], which have given an insight in the evolution of the plasma. However, important questions remained; Through what processes is light emitted by the plasma? And even more relevant; Do linked magnetic field lines play a role in the formation of the ring-structure?

Recently measurements have been done by Vasco Ramalho (Leiden University) which exclude the existence of strong magnetic fields in the plasma. However, these rings can still form a basis for linked magnetic structures. For these magnetic fields to be induced, we need to know more about the plasma. The goal of this thesis is to form a better understanding of the processes within and properties of these plasma rings.

We distinguish three stages in the plasma's lifetime. First is the ionization, when the laser-induced breakdown takes place. This stage lasts the first several nanoseconds. Second is the cigar stage, at this stage the plasma appears to form a cigar shaped cloud, with a large variance in shape between plasmas. This stage lasts until 12 nanoseconds after ionization.

In chapter 2 the set-up is described, and the important components are further discussed. Chapter 3 clarifies on the videos made of the plasma, it includes the camera settings and the image processing. Then in chapter 4 we take a closer look to the ionization stage, and the geometry of the laser focus. In chapter 5 the processes underlying the ring formation are discussed. We take a quantitative look at the shape of the plasma. Finally, we measure the spectrum in chapter 7 and from it derive the temperature using Boltzmann analysis.

This research has been done in close collaboration with Vasco Ramalho. We worked together on both the lab-work and the processing of the data. Vincent Kooij has also collaborated greatly when interpreting the results.

Chapter 2

Set-up

The set-up used to create and observe the plasma can be seen in figure 2.1. The laser creates a polarized pulse which can be partly redirected into the beam dumps. The laser creates a plasma as it is focused in the chamber. The light emitted by the plasma is imaged by the lenses on the ICCD.

The subsections each go deeper into a specific part of the set-up and finally the timing system connecting all components is explained.
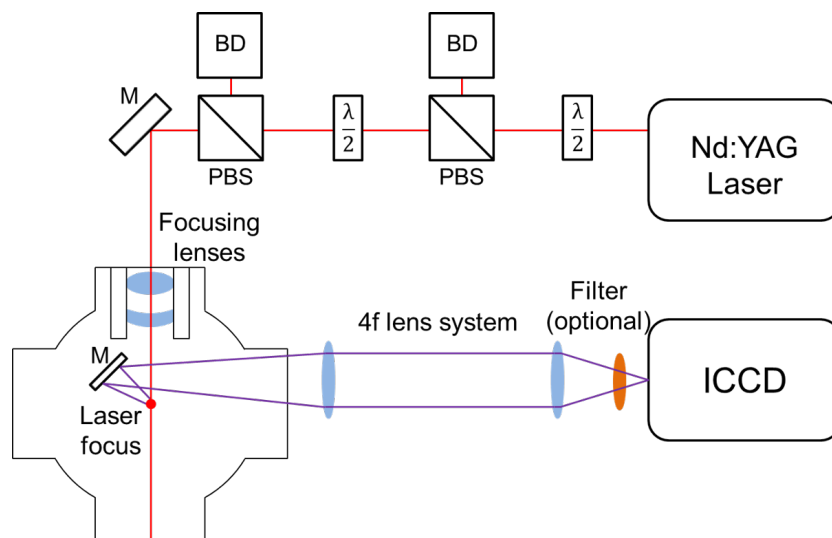
Figure 2.1: *Top view of the experimental set-up, not in scale. The path of the laser pulse is in red and the contours of the imaged light of the plasma is in purple. The abbreviations are; $\lambda/2$: half-lambda plate; PBS: Polarising beam splitter; BD: Beam dump; M: mirror; ICCD: Intensified CCD. This figure is based upon figure 3.1.a from Burgwal 2015 [1].*

9

2.1 Laser

The laser beam used to ionize the Helium is created by a Q-switched Quanta-Ray GCR-3 1064nm Nd:YAG laser, which sends out pulses at 10Hz. It has been shown that the pulse duration is shortest at maximum laser lamp energy [1]. Therefore, in all experiments the lamp energy is set to maximum, giving a pulse duration of approximately 8 nanoseconds. When turning on the amplifier on the laser, a maximum pulse energy of 1 Joule can be achieved. However, the amplifier is usually turned off, and the energy is reduced by attuning the second half-lambda plate, resulting in an remaining energy of 150mJ.

The laser pulse is close to collimated as it reaches the focusing lenses. These lenses have a focal distance of 100mm, focusing the pulse in the center of the plasma chamber. The width of the pulse before the lenses is 8mm, giving a numerical aperture of 0.06.

2.2 Plasma chamber

The plasma is generated inside a vacuum chamber filled with Helium at atmospheric pressure. Helium is used since it is the simplest noble gas. Hydrogen would be too dangerous if any oxygen would enter the chamber. To get pure Helium in the chamber, we first pump the chamber to 2 millibar, after which the chamber is refilled with 99.999% pure Helium. This process is then repeated. The chamber has a radius of about 10cm, with a plasma ring smaller than 1cm the walls should be far enough away to not influence the dynamics forming the ring.

2.3 Imaging system

The produced plasmas can be imaged in two different ways. The first is through a mirror, as shown in figure 2.1, which will be referred to as back view.

Using a 4f lens system the image is magnified and focused onto the ICCD. The distance between the two lenses in the 4f imaging system is in reality smaller than the sum of their focal distances, but since we are only interested in intensity on our ICCD, this does not adversely affect our image quality.

The other way of imaging is by looking directly at the plasma from the side, which will be referred to as side view. For this configuration a single

lens system is used. This mirrors the image horizontally and vertically, but this is corrected when processing the data.

To determine the scale of our images, a target paper with markings is placed at the spot the plasma would be created. Then, by shining a laser beam (or another light source) on the target, it can be imaged. Figure
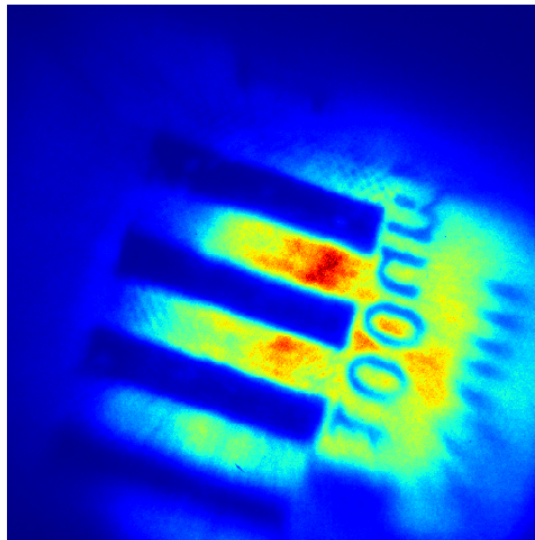

Figure 2.2: *Image of target illuminated by a halogen lamp, imaged through the mirror (back view) using a 4f lens system. The large stripes have a width of 1mm.*

2.2 shows the image of a target. The large stripes have a width of 1mm. Comparing this width to that of the whole image, which consists of 512 pixels, the number of pixels per millimeter is determined. This number differs per lens system, so in the images presented in this report a scale will be added.

Finally, the light is captured by a Roper Scientific PI-MAX camera. This camera detects photons with wavelengths between 200 and 900 nanometers with about 25% quantum efficiency (wavelength dependent). The signal can be intensified by applying a gain. The exposure time has a minimum of 2ns, and the timing can be set with 1ns accuracy. To filter the imaged light a filter can be installed directly in front of the camera.

In front of the camera filters can be attached.

2.4   Timing
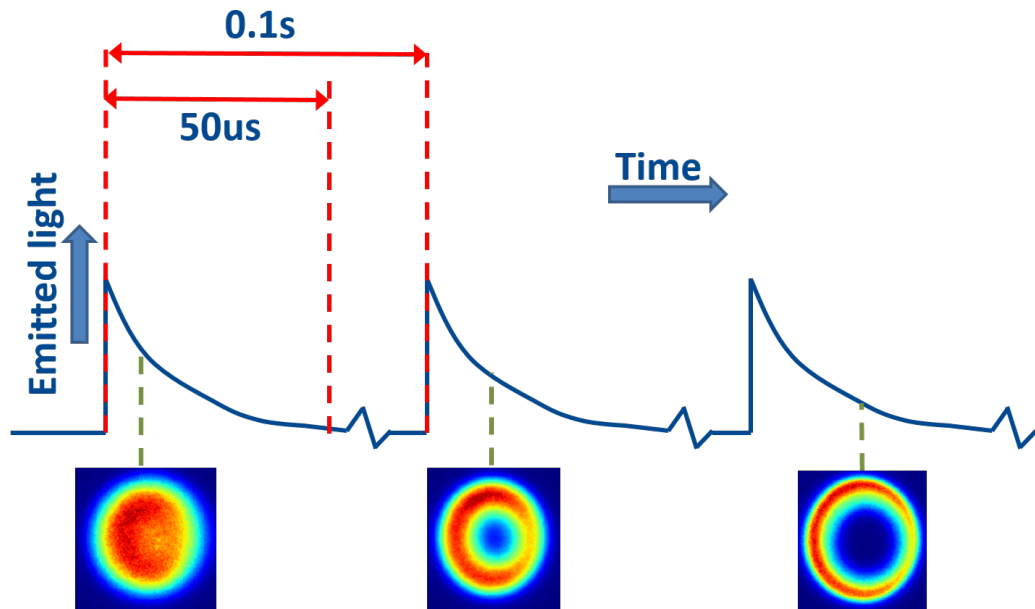
Figure 2.3: *Illustration of the timing in the measurements.*

The timing is an important aspect of the measurements, an illustration can be seen in figure 2.3. Every tenth of a second a laser pulse is emitted and a plasma created. The plasma is then intense enough to be imaged by the camera for approximately 50 microseconds. The camera is not fast enough to take multiple images during one plasma, so to measure a time-evolution each image is taken from a different plasma, each at a different delay time for the camera exposure. Note that in figure 2.3 an image is taken every plasma, while in reality the data read-out of the camera takes about two seconds, so many plasmas are skipped.

Chapter 3

Videos

Videos of the plasma have been made using the set-up described in last chapter. The light emitted by the plasma at its different stages gives a general idea of how the plasma is created and a ring is formed. The videos cannot give a full explanation, but this will be given in later chapters. It is important to keep in mind that every image is re-normalized, in order to keep the plasma visible. In reality the luminosity of the plasma drops five orders of magnitudes from ionization to 30 microseconds.

The videos and their specifications can be found online with the link

goo.gl/MqobD0

The video 'Video side ionization single exp of 2ns' shows the initial ionization of the plasma from the side view. The plasma is seen to expand as two lobes, of which the geometry is investigated in chapter refionization. After this the plasma thickens, becoming cigar-shaped.

The video 'Video back ring 20 exp of 100ns' shows the formation of the ring from the back view. It can be seen that the ring-shape is stable for multiple microseconds. The processes underlying the ring formation are discussed in chapter 6. 'Video side ring single exposure of 20ns' shows the ring from the side view.

3.1 Fluctuations

The cigar stage is shown in 'Video side cigar single exp of 2ns' from the side view. In this video the plasma appears to fluctuate a lot, which has two reasons. First is the difference between each separate plasma. Each

13
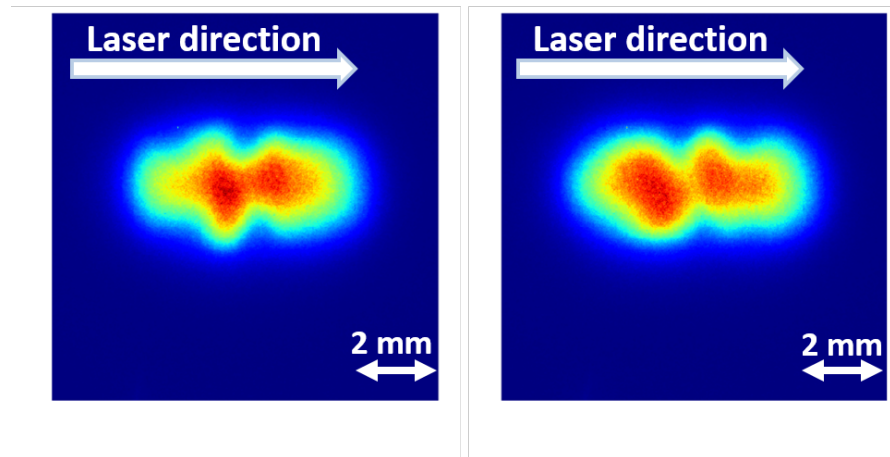
Figure 3.1: *Single exposures of 2 nanoseconds captured by the ICCD at 3.4 microseconds after ionization. The two images are obtained equivalently but are of different plasmas.*

image is taken from a different plasma, if these are not similar, their differences will show up as fluctuations between time-steps. Figure 3.1 shows images of two separate plasmas, taken with the same timing. The two plasmas are clearly not the same.

To account for this effect each time-step is taken to be the average image of multiple plasmas. 'Video side cigar 20exp of 2ns' shows the obtained video. However, still a lot of the fluctuations are seen, meaning they arise in another fashion.

The shape of the image is affected by shock-waves in the plasma which deform the density, and thus the luminosity, of the plasma. These shock-waves will be described further in chapter 5.

The time between each image is 100ns, while the exposure time is only 2ns. In these 100ns the shock-waves evolve and deform the plasma, resulting in a different shape each image. To confirm this, a video is made with 20ns exposure time. Indeed in 'Video side cigar single exp of 20ns' the fluctuations are seen to be less. This indicates that very fast processes are at play during the cigar stage, possibly the interference between the shock waves.

Chapter 4

Ionization

4.1 Laser-induced breakdown

The ionization of the Helium is done by laser-induced breakdown, which depends on two processes [6]. First there is multi-photon ionization. To free an electron from a Helium atom about 25eV is needed. We use 1064nm light, which means 21 photons are needed for ionization. Classically this is process is impossible, but through virtual states of the Helium atom it is possible. The virtual states can exist through the energy-time uncertainty relation. However, the lifetime of these states is very short, so a very high density of photons is needed to ionize the Helium.

Luckily, multi-photon ionization (MPI) is made easier through resonant states, which act as a long-lifetime platform splitting the process in two. First, the helium is excited to the resonant state (1s2p) using 18 photons. Then only 3 are needed to ionize it. The threshold for multi-photon ionization is of the order of $10^{11}W/cm^2$ [6]. While our laser pulse has an energy of $150mJ$, spread over $8ns$ giving a power of $2*10^7W$. The beam waist is about 6 micrometer, meaning the beam will be spread across an area of $30\mu m^2$. This gives the average intensity in the focus to be about $10^{13}W/m^2$. The maximum intensity is even higher than the average, but our focus is not perfect making the average a good approximation. From these values we see that MPI is bound to happen since the threshold is exceeded by a factor 100.

Once free electrons are created, the second process of electron cascade kicks in. Free electrons are accelerated by the intense electrical fields of the laser pulse. As they collide with atoms, energy is transmitted, ionizing new atoms and creating more free electrons. The new free electrons then also accelerate and ionize more atoms. After initial free electrons are cre-

15

ated through MPI, this cascade process ionizes all the Helium in the volume where the intensity is high enough for this cascade to be sustained. Since this process is dependent on electron-ion collisions, it is highly dependent on pressure, giving the following relation [6];

$$I_{th} \sim \frac{1}{P} \qquad (4.1)$$

where I_{th} is the threshold intensity needed for electron cascade and P is the pressure.

4.2   Initial ionization

To better understand the plasma we are dealing with, we look at the moment it is created, which is when the laser pulse reaches its focus and the Helium is ionized.
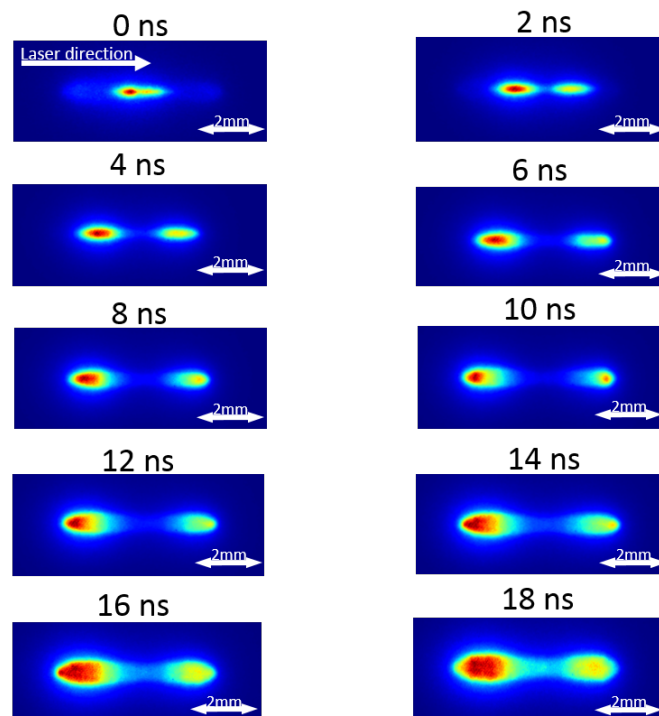
Figure 4.1: *Time evolution of the light emitted by a laser-induced plasma in Helium using a 140mJ pulse, t=0ns is chosen as the delay-time at which the plasma is first visible. Images are single exposures of 2ns duration. Every image is renormalized.*

Figure 4.1 shows images of the plasma at its earliest stage. In the images, the more red the color, the higher the intensity captured by the CCD. Furthermore each image is re-normalized.

The temporal profile of the laser pulse resembles a Gaussian. As time increases, the intensity at the focus increases until it exceeds the threshold for MPI, at which electron cascade takes over and forms an initial plasma. This is set as time 0. As time progresses further, the intensity of the laser still increases, extending the volume in the focus where the electron cascade threshold is exceeded. Notice that from 2ns onward, two spots can be distinguished. This is due to the laser geometry, as will be discussed in the next section. Another important observation is that the second lobe is always smaller and less bright than the first, this asymmetry turns out to be crucial for the ring formation.

Eventually the laser pulse is beyond its peak and the intensity drops again. No more plasma is created (6-8ns), and the plasma starts to expand. The observed expansion after 8ns is also caused by the re-normalization of each image, making less intense regions more visible as time progresses.

4.3   Dual lobe geometry

In 4.1 two spots are visible, while there is only one laser focus. To explain this a closer look is taken into the geometry of a focused Gaussian laser beam.

4.3.1   Theory

Figure 4.2 illustrates the geometry of a focused Gaussian beam. The image should be seen as rotated around the z-axis, as the image shows the distribution in a vertical slice through the focus. Along the r-axis the intensity distribution of the beam is a Gaussian, of which the width changes along the z-axis, being the narrowest at the focus. This means that the intensity is highest in the center of the focus, so one might expect to detect the most light emitted from the plasma at that location. This is, however, not the case as seen in figure 4.1. When detecting the light emitted by the plasma, what is actually detected by the camera is the light emitted along the optical path as given by the green dotted line.

Helium is ionized where the intensity exceeds a certain threshold (red line in figure 4.2). As it exceeds the threshold for electron cascade, almost all atoms will be ionized. As the Helium is ionized, it partly recombines to excited Helium, emitting light as it relaxes. So the light emitted by the
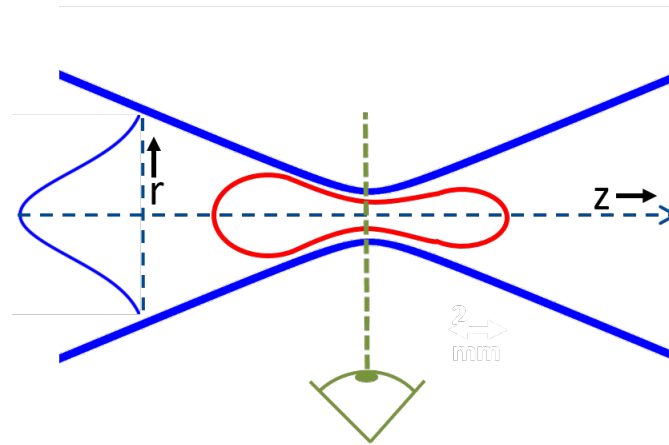
Figure 4.2: *Illustration of a focused Gaussian beam in 2D. The intensity distribution perpendicular to the beam propagation is a Gaussian, of which the width changes with the distance from the focus as a hyperbola. The area at which the intensity exceeds a certain threshold is given by the red line. The beam enters from the left, resulting in a smaller right lobe due to extinction.*

plasma is proportional to the density of atoms, which is still homogeneous given the time-scale of mere nanoseconds. This means the detected intensity is a measure for the amount of ionized helium along the optical path. Note that the local intensity of the laser beam is not completely irrelevant, since it does increase the temperature.

At the focus the Gaussian profile of the beam is the narrowest, which means the intensity is spread over a relatively small cross-sectional area. Therefore only little ionized Helium is present along the optical path, and thus less light emitted. When moving away from the focus the Gaussian profile is spread out, increasing the amount of Helium that emits light along the optical path. Finally, the Gaussian spreads out so much that the peak intensity is lower than the threshold, and no Helium is ionized.

Note that the right lobe in figure 4.2 is smaller than that on the left. Firstly, as the laser beam enters from the left, the laser is scattered and absorbed by the atoms and electrons. This causes a decay of laser intensity along the z-axis.

Another process influencing the size of the right lobe is laser refocusing. As the first lobe is ionized, free electrons decrease the refractive index, resulting in a faster expansion of the beam, as seen in figure 4.3 taken from Monot et al. [5]. Although their experiment differs from ours in terms of pressure, wavelength and pulse duration, the effect of laser refocusing should be considered when analyzing our data.
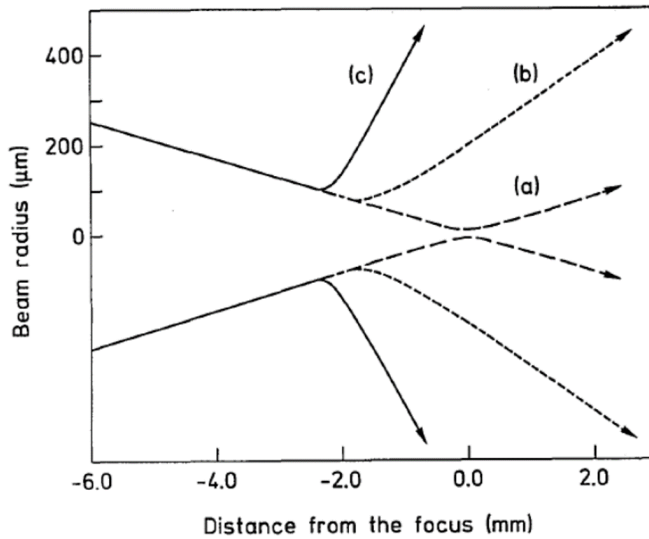
Figure 4.3: *Figure 7 from Monot et al. [5] Caustic curves of the beam for an incident power of 0.1 TW and for several argon pressures: (a) p = 10 mbars, (b) p = 100 mbars, and (c) p = 1 bar. The intensities reached at the focus point are (a) $I = 10^{17}W/cm^2$, (b) $I = 8 * 10^{14}W/cm^2$, and (c) $I = 4x10^{14}W/cm^2$*

We investigate the effect of extinction and laser refocusing by analyzing a simple model taking into account only the beam geometry and extinction. We find that this simple model quantitatively explains many of the observed phenomena, but not all observed phenomena can be explained without laser refocusing.

4.3.2 Model

Using python a simple model is made only taking into account the geometry of the laser beam. The code used can be found under 'data01/qo/zwaan/plasma shape code' in the database of the LION institute. The model is used to investigate the effects of pulse energy and pressure. The results are compared with experimentally obtained data. The intensity is given by the formula

$$I(r,z) = I_0 * T(z) * \frac{1}{1 + \left(\frac{z}{z_R}\right)^2} * \exp\left(\frac{-2r^2}{w_0^2\left(1 + \left(\frac{z}{z_R}\right)^2\right)}\right) \qquad (4.2)$$

where I is the intensity of the beam at horizontal distance z and vertical distance r of the laser focus. In our experiment a $D = 8mm$ wide beam of $\lambda = 1064nm$ light is focused by a lens (n=1.5) with a focal distance of

$f = 100mm$. Giving the following values for the Numerical Aperture NA, beam waist w_0 and Rayleigh length z_R;

$$NA = \frac{n * D}{2f} = 0.06 \tag{4.3}$$

$$w_0 = \frac{\lambda}{\pi * NA} = 5.7 \mu m \tag{4.4}$$

$$z_R = \frac{w_0}{NA} = 94 \mu m \tag{4.5}$$

I_0 is the intensity at the center of the focus, which is approximately $10^{13} W/cm^2$ as derived in chapter 3. I_0 is given by

$$I_0 = 10^{13} W/cm^2 * \frac{E_{pulse}}{260mJ} \tag{4.6}$$

$T(z)$ is the integrated transmission at horizontal distance z. The intensity is calculated from left to right. If no plasma is created yet, $T(z) = 1$. From the position a plasma is created (z_0), $T(z)$ drops exponentially as

$$T(z) = \exp\left(\frac{-(z - z_0)}{E(P)}\right) \tag{4.7}$$

Where $E(P)$ is the length for which $T(z)$ drops a factor of e. It depends on pressure (P) since the density of atoms affects how much the light is extinguished. We assume this relation to be linear. The value of $E(P)$ for atmospheric pressure has been chosen so that the ratio between the heights of the left and right peak approximately match experimental data, giving

$$E(P) = 2.5mm * P[bar] \tag{4.8}$$

The threshold intensity for plasma creation for atmospheric pressure is set such that the size of the plasma matches the experimentally found size, which was found to be $10^{10} W/cm^2 = 10^{-3} I_0$. This is one order of magnitude below the threshold for multi-photon ionization, which indicates this is indeed the threshold for electron cascade.

As described in section 4.1 the threshold depends on pressure, giving the threshold intensity

$$I_{th} = \frac{10^{10} W/cm^2}{P[bar]} \tag{4.9}$$

The output for the model is the intensity of the light emitted by the plasma. At constant pressure, this is simply given by the optical path-length through ionized Helium. But if pressure changes, so does the density of atoms along this path, meaning less atoms emit light. We assume the relation between luminosity and pressure to be linear.

4.3.3 Results and interpretation
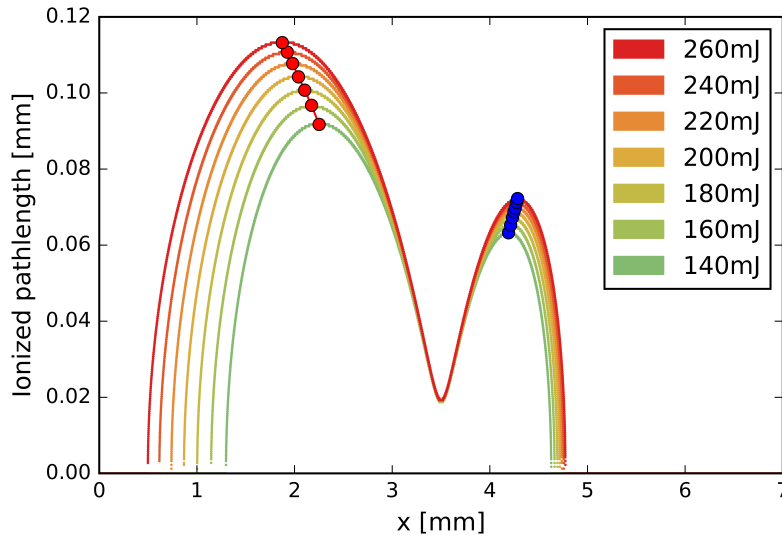
Figure 4.4: *Ionized optical path-length for various energies. The red orbs are the positions of the left peak, and the blue for the right. Laser direction is from left to right.*

Figure 4.4 shows the result of the model for varying the pulse energy at a pressure of 1 bar, while figure 4.5 shows the experimental results obtained by taking the intensity measured by the row of pixels through the center of the plasma.

Comparing the two figures we see that the model properly predicts the existence of two lobes. Also, the change in peak positions is similar to that in the experiment. As the energy is increased, the whole threshold area is expanded. So it is to be expected that the two peaks then move away from the focus.

The result of the model differs from the measurements firstly by the variation in the height of the peaks. When comparing the lowest energy to the highest, the ratio between the peak height is much smaller in the model than in the experiment. Another notable difference is that the dip at the focus is much sharper in the model.

Both differences can be explained by the fact that the model only takes into account the optical path-length through the plasma, while in the experiment we measure the light emitted. The model does not account for the way the laser intensity above threshold affects the measured intensity.
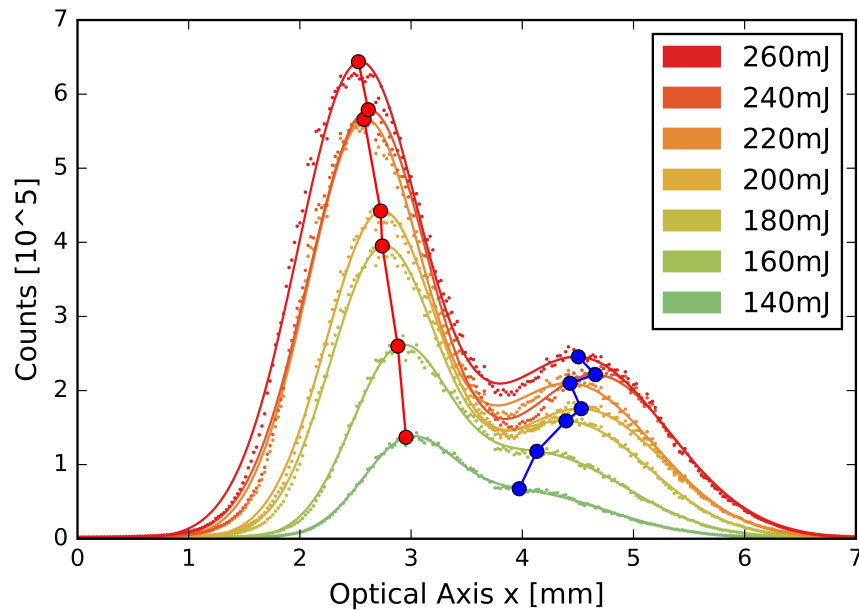
Figure 4.5: *Luminosity of experimental plasma along a slice through the center of the plasma at an approximate delay time of 2 ns, for various energies at a pressure of 1000mbar. The dots represent the experimental data and each line is a fit to the data using a double (two summed) Gaussian(s). The peaks of this fit are given by the red (left) and blue (right) orbs. Laser direction is from left to right.*

Furthermore, the edges of the plasma in the model are sharp compared to the smooth edges found experimentally. This is because in the model nothing happens below threshold intensity, while in reality the Helium will still be partly ionized and thus emit a small portion of light.

Figure 4.6 shows the result of the model for varying the pressure inside the plasma chamber at an energy of 220 millijoules, while figure 4.7 shows the equivalent experimentally obtained data by looking at the row of pixels through the center of the plasma.

When comparing the two figures, again we see the existence of two peaks, with the right peak being smaller. The behavior of the left peak is also properly predicted by the model. However, the behavior of the right peak is not predicted by the model. In the experiment, when going from 600 to 700 millibar, the peak shifts to the right. The peak location has been determined by fitting a double Gaussian. However, the intensity measured does not resemble two peaks anymore, since the right one is barely visible. This results in a high uncertainty in the peak position.

More interestingly is the trend observed in the right peak from 900 to
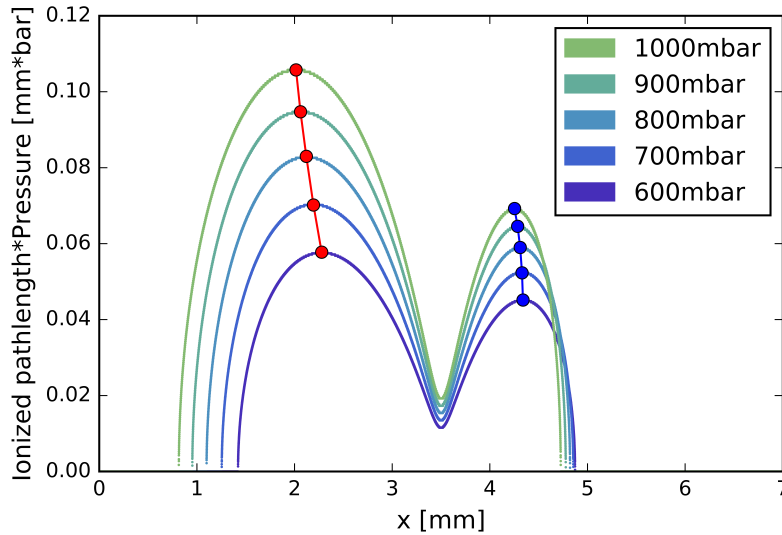
Figure 4.6: *Ionized optical path-length for various pressures. The red orbs are the positions of the left peak, and the blue for the right. Laser direction is from left to right. The results has been multiplied by their respective pressures.*

1000 millibar, as it shifts closer to the laser focus. In the model, this peak also shifts slightly to the left as a result of increasing extinction, but this is not nearly enough to fully explain it. This indicates that to some extent laser refocusing needs to be taken into account.

4.3.4 Discussion

Despite being such a simple model, it is capable of effectively capturing many of the observed phenomena. This indicates that the observed plasma shape is predominantly caused by the beam geometry, a fact that is often overlooked in literature. It is not mentioned by Goshand Mahesh [2] and Leela et al. [3] explain the two lobes by aberrations in the focusing lens. There are other points worth mentioning that our model does not take into account.

The first is the use of a Gaussian beam profile in the model, since the pulse used in the experiment is not fully Gaussian [1]. However, we suspect that the deviations in the beam profile do not have a notable effect on the eventual plasma created, and definitely not on the behavior of the peaks.

A second point is the width (vertical axis in figure 4.4 of the two lobes.
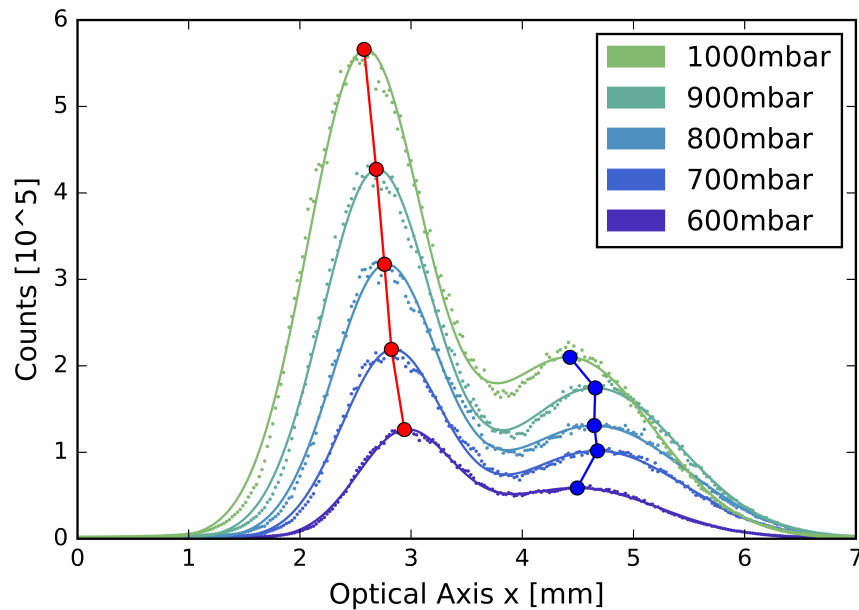
Figure 4.7: *Luminosity of experimental plasma along a slice through the center of the plasma at an approximate delay time of 2 ns, for various pressures at an energy of 220mJ. The dots represent the experimental data and each line is a fit to the data using a double (two summed) Gaussian(s). The peaks of this fit are given by the red (left) and blue (right) orbs. Laser direction is from left to right.*

In 4.1 it can be seen that at 2ns the plasma is at least 0.5mm wide, while the model predicts only a width of 0.1mm. The most probable explanation is that the model assumes nothing happens below threshold intensity, while actually, as explained above, this is not the case.

4.4   Ghost light

When imaging the plasma, a signal was observed on the images taken at a time directly before the ionization. This signal was found to have a much lower intensity than the actual ionization. This observation cannot be explained by our current knowledge of the formation process, and is referred to as 'ghost light'.

Figure 4.8 shows an image captured by the camera at 10 nanoseconds before the ionization is visible. The intensity is approximately 70 times weaker than that of the actual plasma. The captured image also shows the dual lobe geometry, which indicates it might be caused by laser-processes preceding ionization. Also, the ghost light has the same size as the plasma.
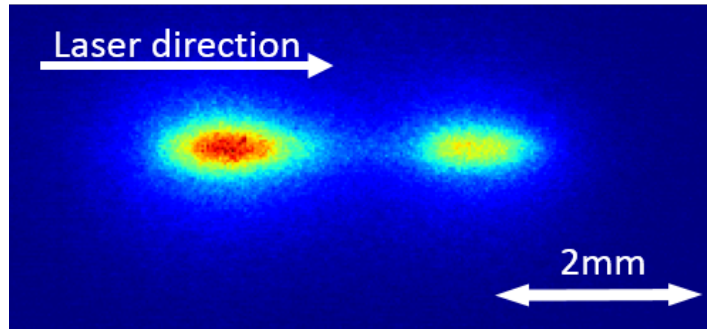
Figure 4.8: *Ghost light imaged at a delay time 10 nanoseconds before the first light of the plasma can be detected, using an exposure time of 2 nanoseconds.*
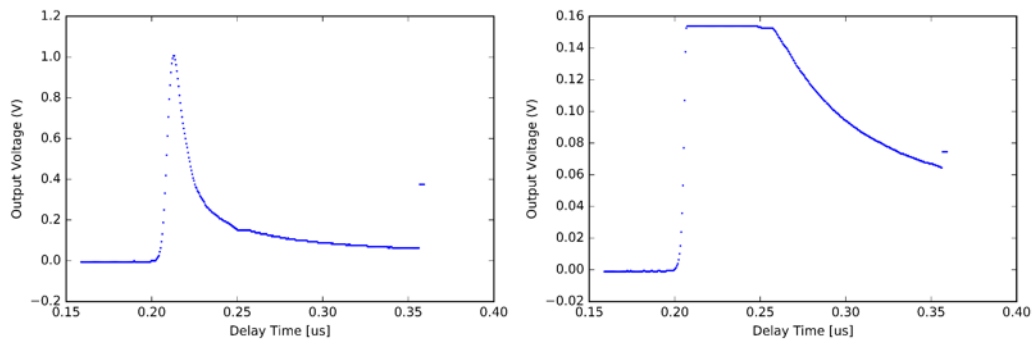
Figure 4.9: *Average intensity of 100 plasma sequences measured by the PDA10A Si photodiode (left) and the same measurement vertically zoomed in (right). Delay times are not equivalent to those of earlier graphs.*

However, the laser pulse lasts 8 nanoseconds, while the ghost light is visible 10 nanoseconds before the actual plasma.

To test whether the ghost light is a real phenomena, the camera is replaced by a 400 micrometer multimode fiber, leading to a THORLABS PDA10A Si photodiode. Measuring the intensity with the photodiode excludes any effects from camera electronics. When aligning the photodiode with the fiber, it was purposely put out of focus. First of all to prevent overexposure, but also because this way we do not just capture light from on part of the plasma, which might be a part where ghost light isn't detected. Instead, we capture light from a large area, which must include the ghost light's area.

Figure 4.9 shows the photodiode signal averaged over 100 traces. The signal was captured by an oscilloscope which was triggered by the laser timing signal. The plasma is visible from 0.21 microseconds delay time, while before this was corrected to be at time 0. The peak output voltage

can be seen in the left image, which is around 1.0V. The signal captured by the camera before ionization is 70 times weaker than light emitted by the plasma, but the photodiode does not detect any signal, even at the 0.02V level,. Whereas if the light was real, a signal of $\frac{1}{70}$V, almost 10 times larger than 0.02V, would be expected.

From this result can be concluded that the ghost light is an artifact of the camera. We hypothesize that it is caused by the gating pulse applied to the ICCD, which is activated by a short high voltage pulse applied to a microchannel plate. Any ripple on this pulse after the pulse is terminated could result in a (small) signal just before the camera is exposed to light.

5 Chapter

Ring formation

5.1 Experiment

Shadow imaging measurements have been done by Vasco Ramalho, of which the setup can be seen in figure 5.1. The 5mW 632.8nm HeNe laser beam is sent through a polarizer and the plasma. The density gradients deform the beam profile. The laser light is then imaged on the ICCD by a 4f imaging system with the imaging plane through the plasma. Light other than the laser light will be blocked by a 632.8nm bandpass filter.

The results of these measurements can be seen in figure 5.2. The light of the laser has been measured for different times around and after ionization. The colors in the images give the intensity captured by the camera, purple is low and red is high.

As the laser pulse creates the plasma, energy is absorbed. However, since the pulse is only 8ns long, the gas density does not change much. This results in an increase in temperature and pressure, located in the two lobes as described in dual lobe geometry. The two hot cores expand at super sonic speed, creating a high density shock-waves around the plasma and a low pressure area within. The pressure variations in the shock-waves deform the laser beam, creating the structures visible in figure 5.2.

At 30ns the structure resembles the dual lobe geometry, after which it starts to expand. Interestingly, at 160ns the right lobe appears to be bigger than the left, while in the dual lobe geometry the left lobe absorbs more energy. As explained by Gosh and Mahesh [2], this asymmetry results in a larger initial temperature in the left lobe. The temperature in the left lobe decreases faster, resulting in the expansion eventually becoming stronger in the right lobe.

The speed at which the shock-waves travel through the plasma is de-

27
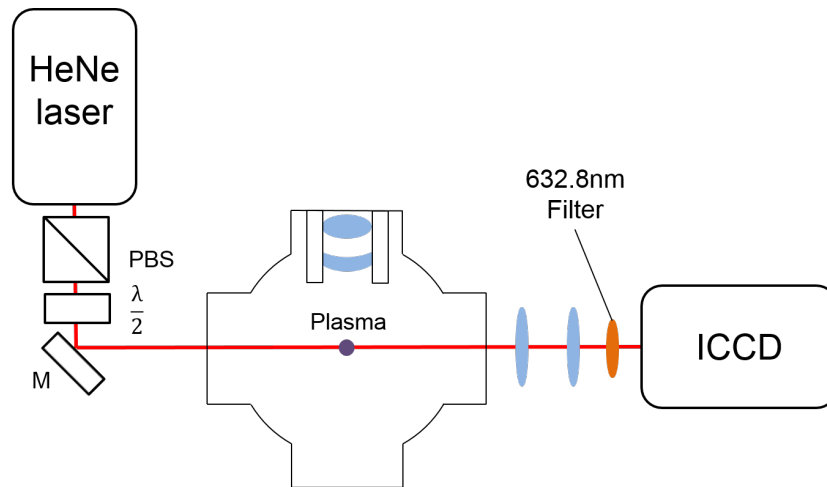
Figure 5.1: *Set-up for shadow imaging, the HeNe laser has a power of 5mW, of which the polarization can be set by the half-lambda plate. The laser travels through the plasma and is imaged on the ICCD. The filter filters out all wavelengths other than 632.8nm.*

termined between the times of 300ns and 480ns. The distance between shock-wave fronts along the laser propagation axis is determined from figure 5.2. At 300ns this distance is 0.46mm and at 480ns it is 0.54mm. This gives an expansion of 0.08mm in 180ns, yielding a speed of 0.44km/s. The speed of sound in Helium at room temperature and atmospheric pressure is 1.0km/s. The shock-waves thus expand at a speed of around half the speed of sound, which is unexpected since shock-waves are believed to be super-sonic. The speed perpendicular to the laser propagation is determined equivalently, yielding a speed of 0.47km/s.

5.2 Comparison to LIP in air

Density fluctuations at ring formation (14us) are not strong enough to be visualized in our set-up. However, Leela et al. [3] have done similar experiments on laser-induced plasma in air using an interference set-up that is much more sensitive to density fluctuations. Their results can be seen in figure 5.3.

Here (a) to (e) show structures similar to those in figure 5.2. While further images show the creation of a jet which is formed by the collapse of the right high density shell. The right hot core collapses earlier than the left, after which a jet is formed that travels through the plasma.

Note that the time-scales are different from our experiment. In Helium
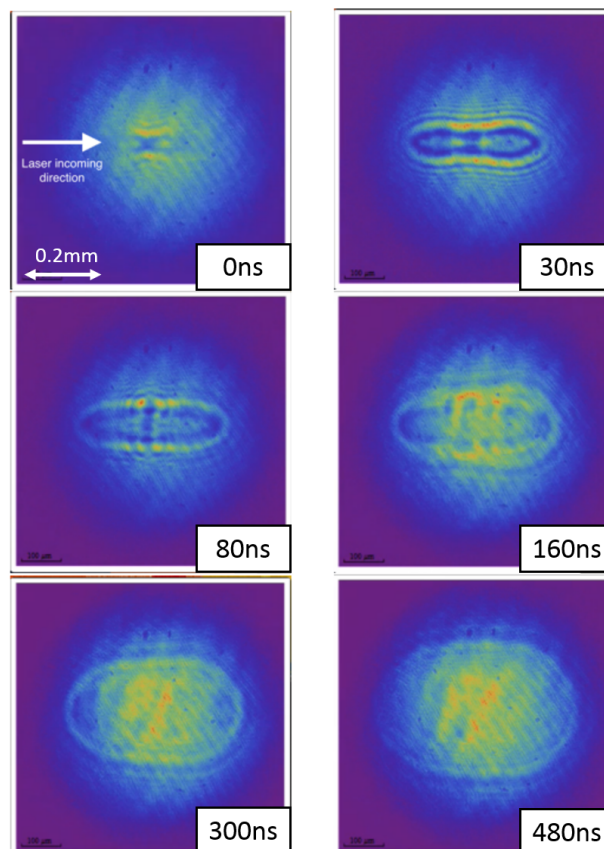
Figure 5.2: *Shadow images measured by the set-up described in figure 5.1, for times of 0, 30, 80, 160, 300 and 480 nanoseconds after ionization. In the images a red color indicates more light being captured by the camera. The laser comes in from the left.*
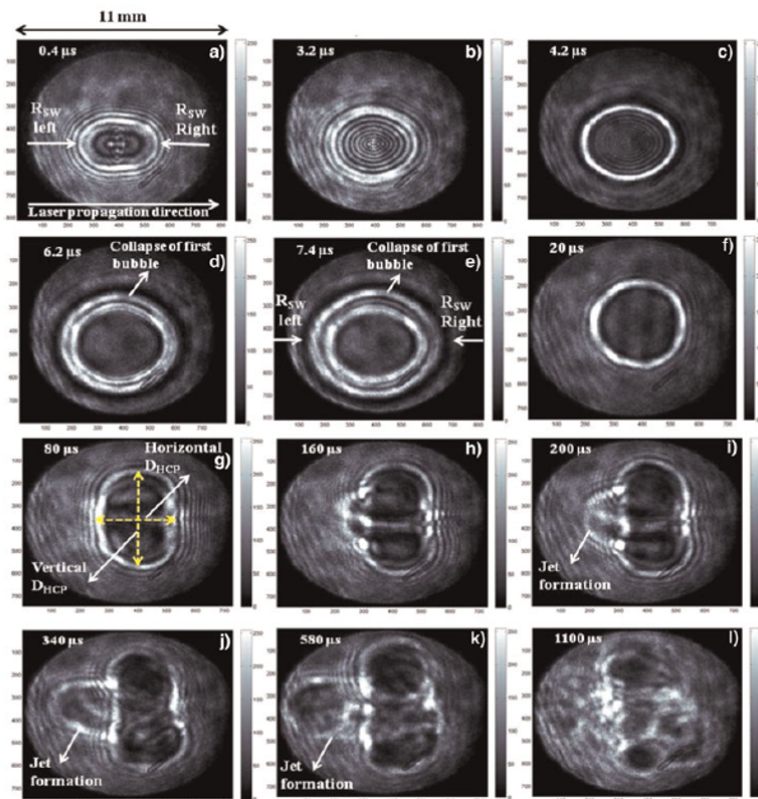
Figure 5.3: *Figure 2 from Leela et al. [3]. Shadowgraphs showing temporal evolution of shock-waves (SW) and hot core plasma (HCP) of air at (a) 0.4 us, (b) 3.2 us, (c) 4.2 us, (d) 6.2 us, (e) 7.4 us, (f)20 us, (g)80 us, (h) 160 us, (i) 200 us, (j) 340 us, (k) 580 us, and (l) 1100 us at 50 mJ input laser energy. Each image represents a spatial extent of 11x11 mm with a resolution of 13x13 um.*
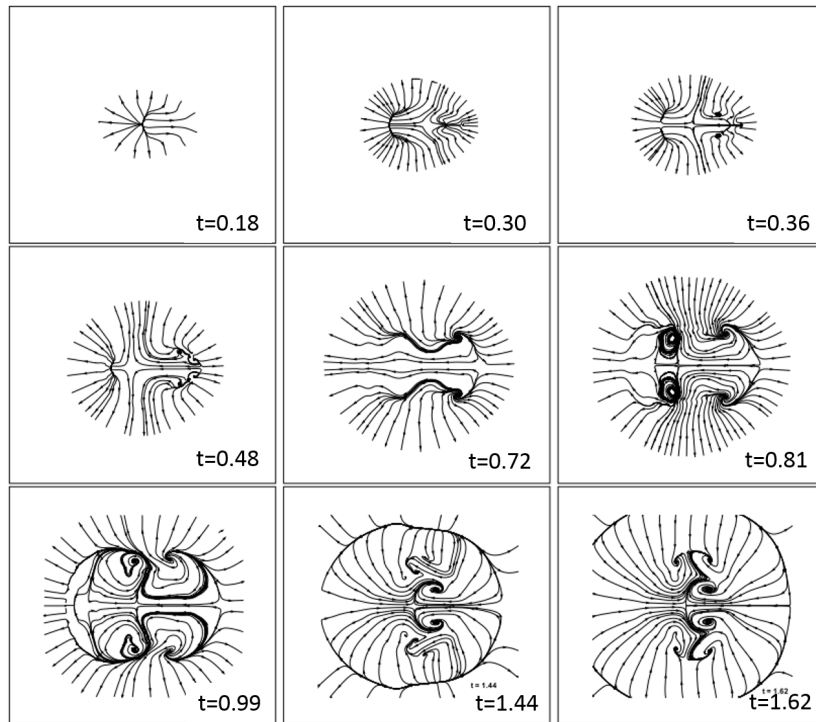
Figure 5.4: *Figure 6 from Gosh and Mahesh [2]. Simulation of a laser-induced plasma, visible are the velocity streamlines of the fluid.*

the ring is formed after approximately 14 microseconds, while in air it takes at least 200 microseconds before a jet is formed. An explanation is the higher mass-density of air compared to Helium, which slows down the fluid dynamics.

The jet formation does not yet explain how the ring is formed and why it remains stable for tens of microseconds. Simulations done by Gosh and Mahesh [2] give an insight in the motion of the fluid as it forms a ring.

5.3   Simulations

Ghosh and Mahesh [2] conducted simulations on the effects of laser-induced breakdown in air. They start with a tear shaped temperature profile, out of which two hot cores are formed. Figure 5.4 shows the computed velocity field of their simulation.

Before $t = 0.48$ the two hot cores are expanding. Asymetry between the two expansion cores causes a flow from the left to the right core. As the right core collapses first, the jet is formed and fluid rushes in from right to

left. The combination of these opposing flows pushes the plasma in radial directions while creating vortices. These vortices form a ring, as the center is replaced with less ionized Helium from the edges of the plasma.

5.4   Conclusion

These results allow us to explain the formation of the ring with purely fluid dynamics. Combined with the fact that no strong magnetic fields have been measured using Faraday rotation, the effect of linked magnetic fields on the ring formation is excluded.

Chapter 6

Plasma shape

The shape of the final configuration of the plasma, the formed ring, depends on several physical aspects, including the gas pressure.

As seen in the previous chapter, the plasma expands during the cigar stage. As one of the shock-waves collapses a hole is created forming the ring. The processes creating the ring are described by fluid mechanics, which are dependent on pressure. This chapter analyses the effects of pressure changes on the ring being created.

Aspects of the shape of the plasma during cigar and ring stage are quantitatively obtained by processing the images taken by the camera, looking through the back view. We investigate the diameter, hole size and area of the light emitted by the plasma as captured by the camera.

6.1 Methodology

The images captured by the camera have been obtained by using 100ns exposure time (200ns for measurements done at 396 millibar) and with multiple exposures (20-40) on the CCD chip. With these settings the plasma is clearly detectable until 30 microseconds after ionization. Furthermore, multiple exposures average out differences between plasmas, making the measurement more reproducible.

Processing the data is done in python. For each image the maximum intensity is extracted. Then, a threshold is set at half this maximum, the shape being defined as the region as the region where the measured intensity is higher than this threshold. This thresholding process is illustrated in figure 6.1.

The horizontal width of the plasma is given by the distance between

33
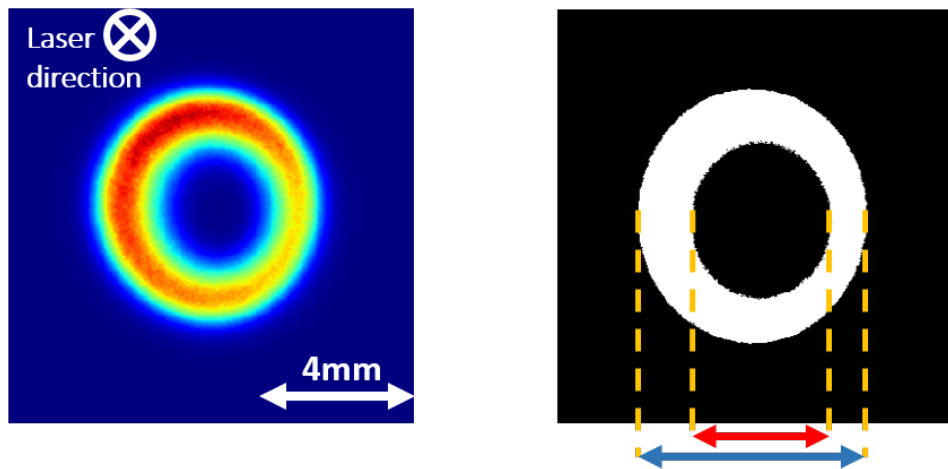
Figure 6.1: *Illustration of processing the data to obtain the shape. Left is an image of the plasma captured at 22.3 microseconds delay through the back view. The right image shows the pixels that have measured an intensity higher than half of the maximum intensity. From this the diameter (blue arrow) and the hole size (red arrow) is determined.*

the most left and most right pixels above threshold. The diameter is then chosen as the maximum of horizontal width. The hole diameter is determined by the distance between the first and last pixel below threshold within this pixel row. If no pixels in this row are below threshold, the hole size is set to zero. The area is given by the total amount of white pixels in the image.

6.2   Results

6.2.1   Atmospheric pressure

Figure 6.2 shows the results of the diameter, hole size and area of the plasma as captured on the camera and processed as explained above. Measurements have been done at a pressure of 1002 millibar in the plasma chamber from 1.4 to 29.2 microseconds delay times from ionization, with steps of 0.2 microseconds.

The diameter is given by the blue dots in 6.2 and can be seen to increase from 5 microseconds onward. The area, given by the green dots, increases until 11 microseconds. But then, as the ring is formed as seen by the red dots indicating hole size, the area stops expanding for a few microseconds.
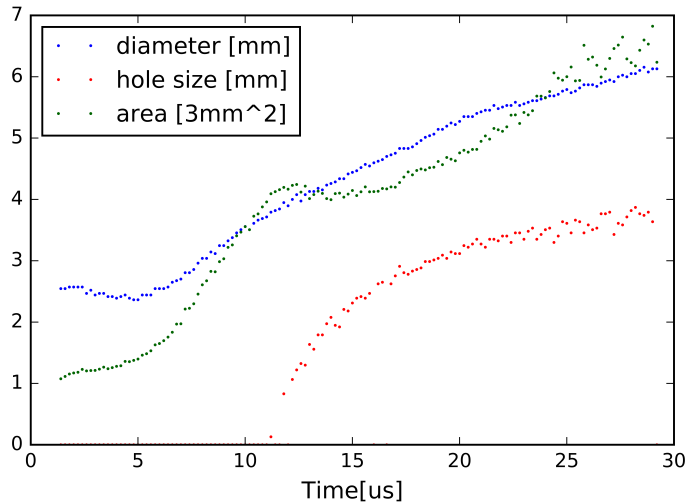
Figure 6.2: *Plasma shape aspects at a pressure of 1002 millibar. The diameter (blue), hole diameter (red) and plasma area (green) are shown. The hole appears at roughly 12 microseconds.*

Now the different aspects of the shape will be investigated individually for multiple pressures.

6.2.2 Multiple pressures

Figure 6.3 shows the diameter of the plasma for multiple pressures. For all pressures, the diameter is seen to increase as time progresses. At the lowest pressure (396mbar) the results become noisy from 25 microseconds onward, which is caused by low intensities measured by the camera. These results should not be seen as an indication of a downward trend, rather this should be contributed to measurement noise.

Interesting is that a lower pressure results in a smaller ring diameter. A possible explanation that at lower pressures, the laser intensity decays slower as it travels through the plasma, as described in chapter 4. This results in less asymmetry between the two lobes, and thus a smaller flow from left to right to counter the flow form the jet formation. This in turn results in the plasma being pushed outward less creating a smaller ring.

Figure 6.4 shows the area above threshold for multiple pressures. Note that in general, lowering the pressure results in a decrease in area. This can be explained by the reduced diameter of the plasma, as the ring detected is smaller.
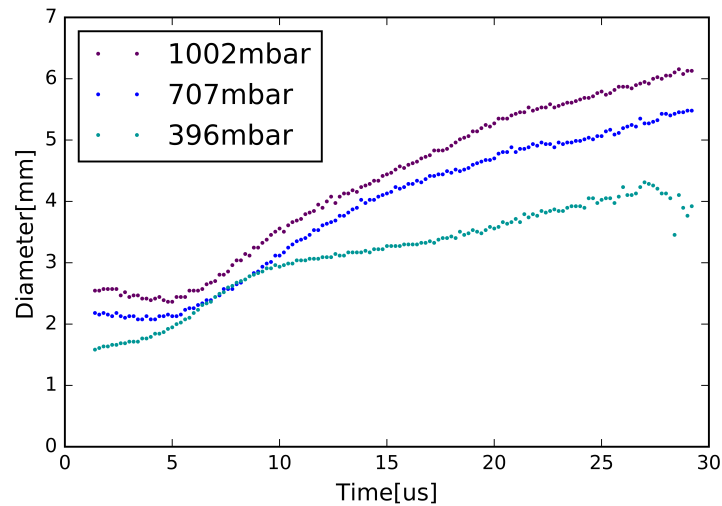
Figure 6.3: *Diameter of the plasma at pressures of 1002, 707 and 396 millibar.*

Also interesting is that for all pressures the derivative of the area changes around ring-formation, which indicates the ring formation has a major effect on the plasma dynamics. This would be expected since as described in previous chapter, the ring formation is caused by flows disturbing the shape of the plasma.

Notable is the behavior of the area after ring formation, for 1002mbar it increases again, while for 707mbar is slightly decreases and for 396mbar it decreases the fastest. An explanation for this has not yet been found.

In figure 6.5 the hole size is plotted for various pressures. Interestingly the behavior of the hole does not vary greatly on pressure. From this can be concluded that the ring formation dynamics are independent of pressure.

6.2.3   Discussion

The behavior of the aspects of the shape of the ring have been investigated for multiple pressures. However, interesting would be to also investigate the shape for multiple laser pulse energies. This would allow us to see how the ring is formed when more energy is deposited in the plasma, and more powerful shock-waves are created.
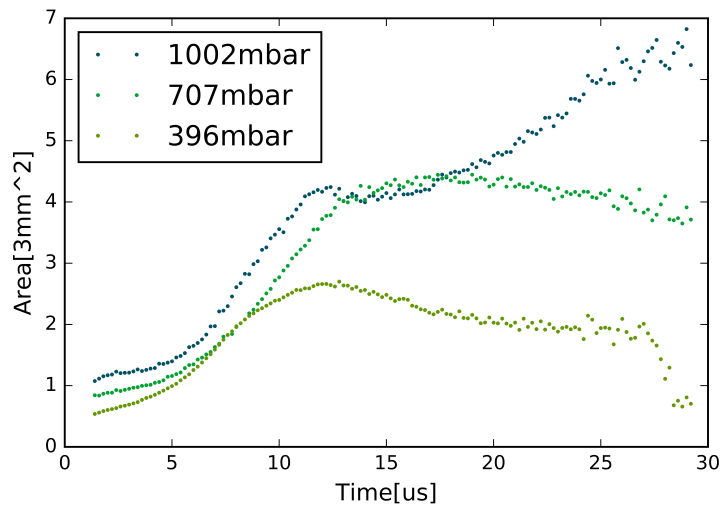
Figure 6.4: *Area of the plasma at pressures of 1002, 707 and 396 millibar. Higher pressures are indicated by a darker shade of green.*
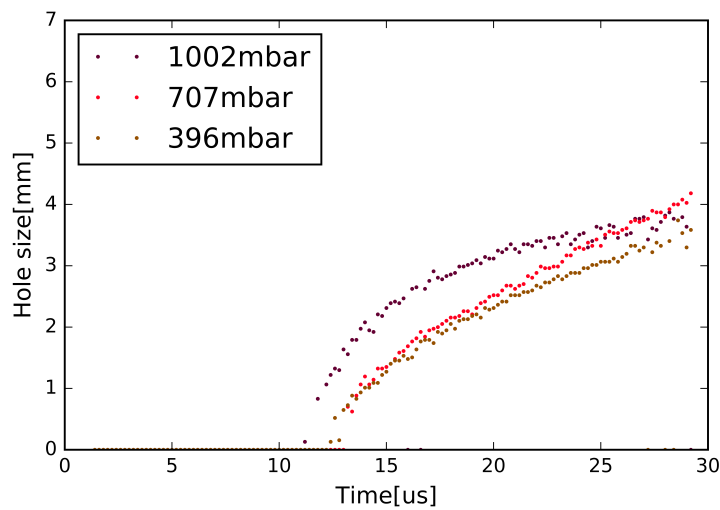
Figure 6.5: *Hole size of the plasma at pressures of 1002, 707 and 396 millibar.*

Chapter 7

Spectrum

The spectrum of the light emitted by the plasma is investigated. First by using band-pass filters to capture certain Helium spectral lines, of this data the temperature is derived using Boltzmann analysis.

Furthermore, a full spectrum is obtained using a prism, which shows a spectral line only emitted by ionized Helium, indicating recombination is still ongoing after ring formation. Also, the spectrum of the emitted light around ionization is studied.

7.1 Filters

A band-pass filter transmits light only in a narrow wavelength range. By installing such a filter, only light within this wavelength range will be detected by the camera. The measured intensities in this wavelength range are then compared to those of the full spectrum detected when no filter is installed. The filters used are shown in table 7.1.

Wavelength [nm]	Transmission	He line [nm]	TR [$10^7 s^{-1}$]
470	0.54	469 (He+)	16
		471	0.32
590	0.57	588	5.4
670	0.70	668	6.4
710	0.55	707	0.93

Table 7.1: *Table showing the filters used (peak transmission wavelength), their transmission at the peak, the corresponding spectral line(s) and their transition rates.*

39
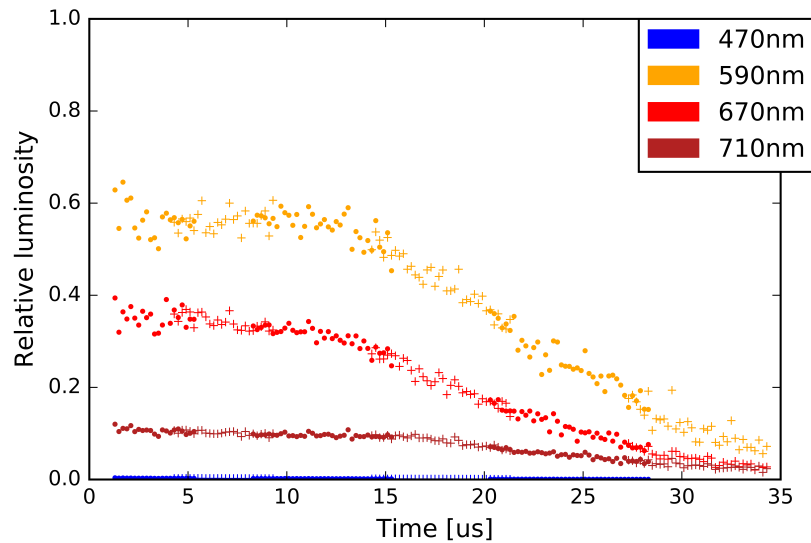
Figure 7.1: *Relative luminosity obtained using various filters. The luminosity measured without filter is set at 1, for every time-step. The luminosity while using a certain filter is then compared to the full luminosity. The dots and crosses are to indicate separate measurement-sequences.*

In table 7.1 the first column shows the central wavelengths of the transmission of the band-pass filters. All filters have a FWHM in transmission of 10 namometers. The second column gives the peak transmission of the filters, which is useful when comparing measurements done with different filters. The third column gives the spectral line of Helium which lies within the transition region of the band-pass filter. The last column is the transition rate of the transition which produces the spectral line, taken from the NIST database [7]. If the line is produces by more than one transition, the average transition time is taken.

Note that within the transition region of the 470nm filter, there are two spectral lines. The one we wish to investigate is the 469nm line of He+, but we cannot distinguish it from the 471nm line of neutral Helium. This last line however, is only created by very weak transitions. The highest transition rate being $5.3 * 10^6 s^{-1}$, while that of the He+ line is almost two order of magnitudes higher at $2.2 * 10^8 s^{-1}$.

For each time-step, an images are taken with and without filter. For both imaged the total luminosity is calculated by summing over all pixel counts. The luminosity with filter is divided by the luminosity without filter to obtain the data in figure 7.1.

The dots and crosses indicate different measurement sequences. It is
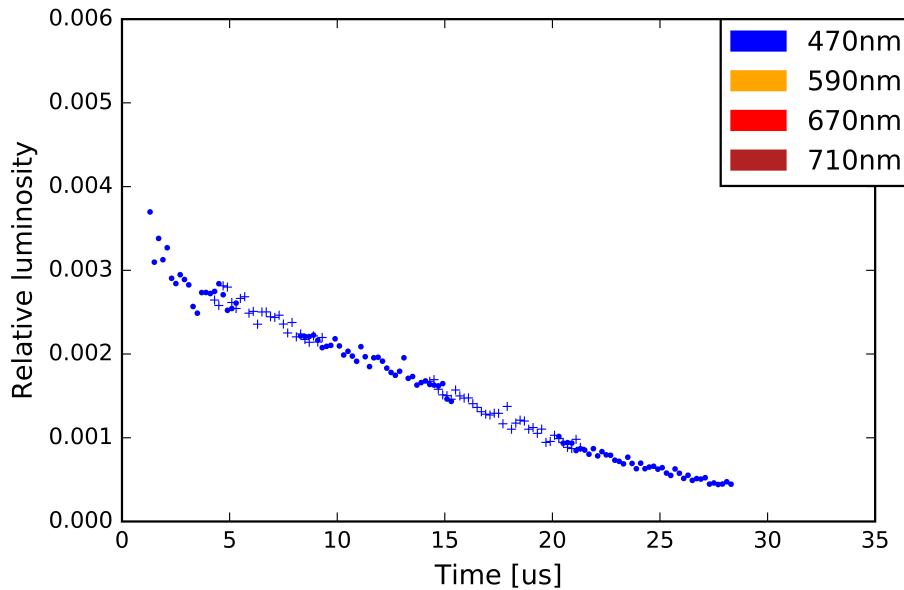
Figure 7.2: *Relative luminosity obtained using the 47nm filter. The dots and crosses are to indicate separate measurement-sequences.*

impossible to measure the luminosity at every time-step maintaining the same camera settings, since the luminosity drops five orders of magnitude in the 30 microseconds after ionization. After each sequence, the gain on the ICCD is increased, which results in an higher luminosity measured. To account for this, an overlap of six images is made between sequences. The total luminosity of these images is determined for both sequences, after which the data from the incoming sequence is corrected by the ratio of the two values, setting its total luminosity equal to that of the outgoing sequence.

In figure 7.1 it can be seen that summing the relative luminosities, approximately 1 is obtain for times before 14 microseconds. This means (almost) all of the light emitted by the plasma is relaxation of excited Helium. Also, the blue dots indicating the light from a transition in He+, are much lower than the other dots indicating transitions in neutral Helium.

However, after 14 us all relative luminosities drop. This indicates there is light being emitted at an wavelength not within the range of our filters. This will be investigated further later in this chapter.

Returning to the results for the 470nm band-pass filter, figure 7.1 is remade with a different vertical scale on the axis into figure 7.2. There we see the luminosity around 470nm is decreasing slowly. The low luminosity compared to the other wavelengths indicates we measured the weak

transition in neutral Helium instead of the He+ transition. Another possible source is the black body radiation, which emits small amounts of light at all detectable wavelengths.

The results obtained by using the filters can be used to determine the temperature of the plasma by applying Boltzmann analysis.

7.2 Boltzmann analysis

The light detected in the previous section was created by relaxation of excited Helium atoms. Excited atoms are created by two processes. First of all, when ionized Helium recombines with electron, excited Helium atoms are made. However, at later stages there is only a limited amount of ionized Helium in our plasma. The second process is thermal collisions between neutral Helium atoms. The energy of these collisions can be used to excite the atoms.

To apply Boltzmann analysis we assume the second process is dominant. Excited Helium can be in numerous states, all with a certain energy and emitting certain light. The key part of Boltzmann analysis is the formula giving the amount of atoms in a certain state, which is

$$P(state) = N_0 \exp\left(- \frac{\epsilon(state)}{k_B T} \right) \tag{7.1}$$

Where P is the population of a certain state, N_0 the population of the ground state, ϵ the energy of the state, k_B the Boltzmann constant and finally T the temperature.

For this formula to apply, thermal equilibrium must be assumed. And importantly, transitions between the states must be predominantly caused by thermal collisions, of which two remarks can be made. First of all, these collisions must be capable of exceeding the energy gap between the ground state and other states. In the Helium atom, excited states are at least 20eV higher in energy than the ground state. At 10,000K, which is a temperature measured before for such plasmas [4], the Boltzmann factor $e^{\epsilon/K_B T}$ for excited states is of the order 10^{-10}, which is extremely low. However, Helium has a meta-stable state at 20.6eV (1s2s) with a lifetime in the order of milliseconds, which can act as the state from which atoms are excited through thermal collisions. Then, the Boltzmann factor becomes of the order of 10^{-2} for the relevant states of which the detected light is emitted. This type of excitation mechanism does not change the result obtained, but is nevertheless important for our understanding of the relevant processes.
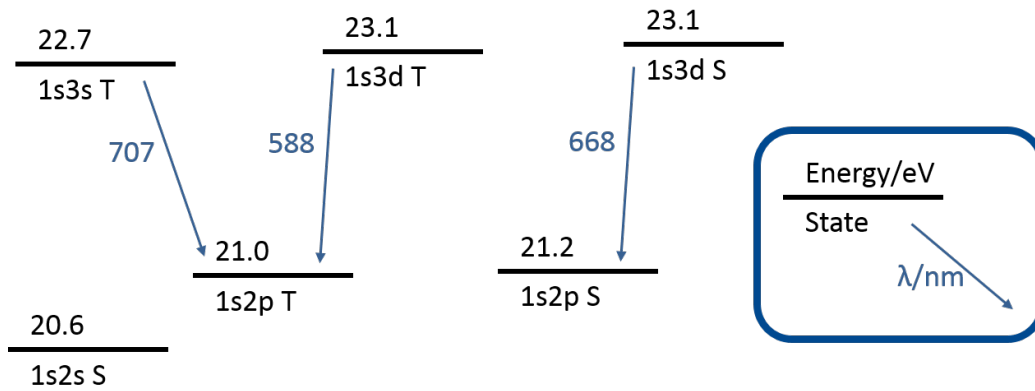
Figure 7.3: *Illustration of the relevant energy levels in neutral Helium.*

Secondly, thermal collisions are not the only cause of transitions between states. Relaxation of excited states brings excited Helium to a lower state. But as long as the thermal collisions are more frequent than relaxation, Boltzmann analysis is still valid. Monafred [4] approximates an atom collides every two nanoseconds for gases at atmospheric pressure at 10,000K. Comparing this to table 1 in [4], the lifetime of the state producing the 588nm light has a relaxation lifetime of 1ns. Which means the 588nm line cannot be used for Boltzmann analysis. The other states do have a relaxation lifetime longer than 2ns.

Figure 7.3 illustrates the energy levels in neutral Helium which are relevant for our analysis. The notation of the states goes as follows. One electron is assumed to be in the ground state, signified by the 1s. The other electron is in an excited state, given by the next two symbols. The T/S stands for whether the electron pair has parallel spin (triplet state T) or anti-parallel spin (singlet state S).

For the 1s2p meta-stable state both the triplet and singlet state act as platforms from which the atoms are excited. Collisions are assumed to neglect transition rules applying for spontaneous decay. In figure 7.3 only the singlet state is shown since it has the highest energy resulting in easier excitation. So most excitations will emerge from the singlet meta-stable state.

The population of states is determined from the measured light by

$$P = C * \frac{L}{TR} \tag{7.2}$$

Where P is the population of the upper state of the transition creating the light. L is the relative luminosity in figure 7.1, TR the transition rate as in
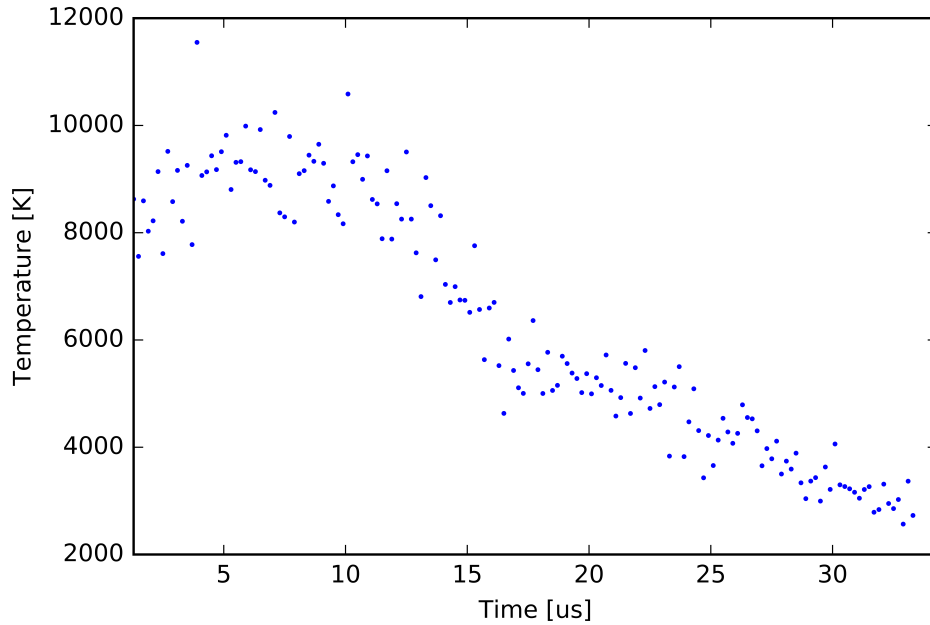
Figure 7.4: *Temperature of the plasma derived using Boltzmann analysis based on the results shown in figure 7.1.*

figure 7.1 and C a factor taking into account camera efficiency, amount of captured light etc. The value of C is unknown, but constant for all the states. Also, the value of N_0 in equation 7.1 is unknown. Both unknowns can be canceled out by taking the ratio of population of two different states, we use the states 1s3s T emitting 707nm light and 1s3d S emitting 668nm light.

$$\frac{P_{1s3sT}}{P_{1s3dS}} = \exp\left(\frac{\epsilon_{1s3dS} - \epsilon_{1s3sT}}{k_B T}\right) \tag{7.3}$$

Rewriting yields

$$T = \frac{\epsilon_{1s3dS} - \epsilon_{1s3sT}}{k_B \ln\left(\frac{L_{707nm}}{TR_{1s3sT}} * \frac{L_{668nm}}{TR_{1s3dS}}\right)} \tag{7.4}$$

From this the temperature is determined for each time-step, the result in shown in figure 7.4. The result is found to be comparable to the temperature found by Monafred [4]. However, before 10 microseconds the temperature appears to be rising, which is very unlikely since no energy is added tot the plasma after the laser pulse. We believe the assumption

of thermal equilibrium is not valid before 10 microseconds, since too little time has passed for thermal equilibrium to settle in after the laser pulse.

From figure 7.1 we see that after 14 microseconds not all the emitted light in within the wavelength bands of our filters. To investigate the wavelengths of the remaining light, we build a spectrometer using a prism and our camera as described in the next section. Also, the spectrum of the light around ionization is studied.

7.2.1 Discussion

The camera's quantum efficiency is dependent on wavelength, affecting the measured luminosities differently for each wavelength. This affects the calculated derived populations used in the boltzmann analysis. However, the Boltzmann analysis is done using the 668nm and 707nm lines, which lie close together. In the next section the wavelength dependence of the efficiency is determined for the prism set-up. It shows the efficiency for the 668nm line is a bit higher than that of 707nm, which would result in a lower temperature if corrected for.

Also worth noting is the difference in luminosity measured with the 590nm and the 670nm filter. As seen in figure 7.3 the upper levels of the transitions causing the 588nm and the 668nm line have the same energy of 23.1eV. So from Boltzmann analysis we would expect them to have an equal population. With transition rates of $5.4 * 10^7 s^{-1}$ for the 588nm line and $6.4 * 10^7 s^{-1}$ for the 668nm line and equal population, more transitions creating the 668nm light would occur. However, figure 7.1 shows a higher luminosity for the 590nm filter than for the 670nm filter. An explanation is the quantum efficiency described above, which is around 20% larger at 588nm compared to 668nm.

7.3 Prism spectroscopy

7.3.1 Methodology

To obtain a full spectrum of the light emitted by the plasma a prism is installed in front of the camera.

As seen in figure 7.5 the light from the plasma passes through vertical slit. The different wavelengths of the light are split by a prism. And the slit is imaged on the ICCD. Every wavelength is imaged on a different horizontal location. The spectrum of the emitted light can now be read from the camera as an horizontal line of pixels.
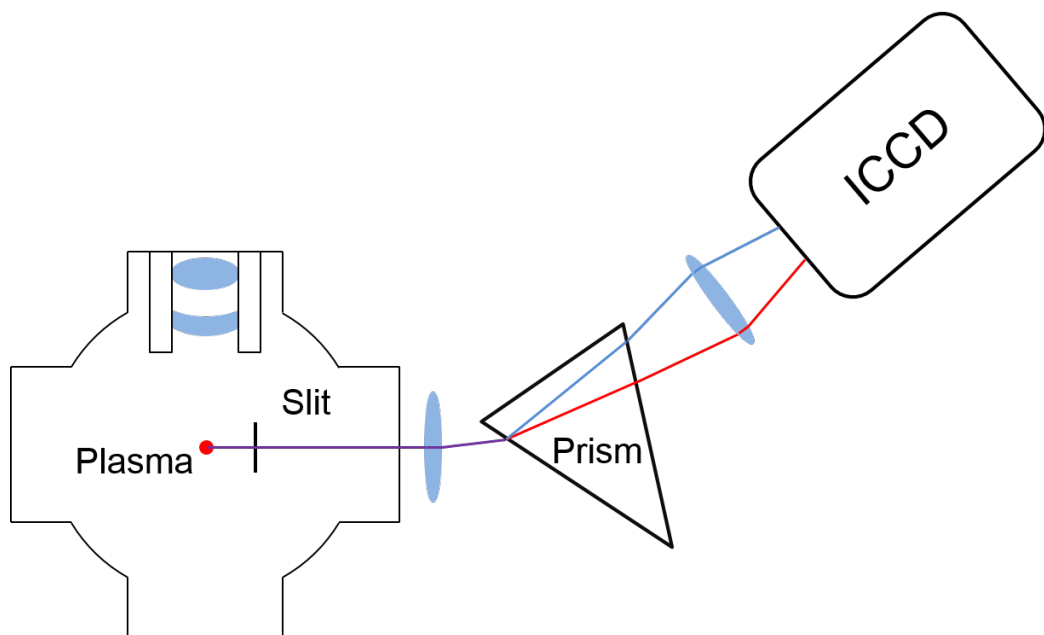
Figure 7.5: *Top view of the imaging system for prism spectroscopy, not in scale. The light form the plasma is given in purple. Different wavelengths travel under different angles through the prism and are imaged on different locations on the ICCD.*
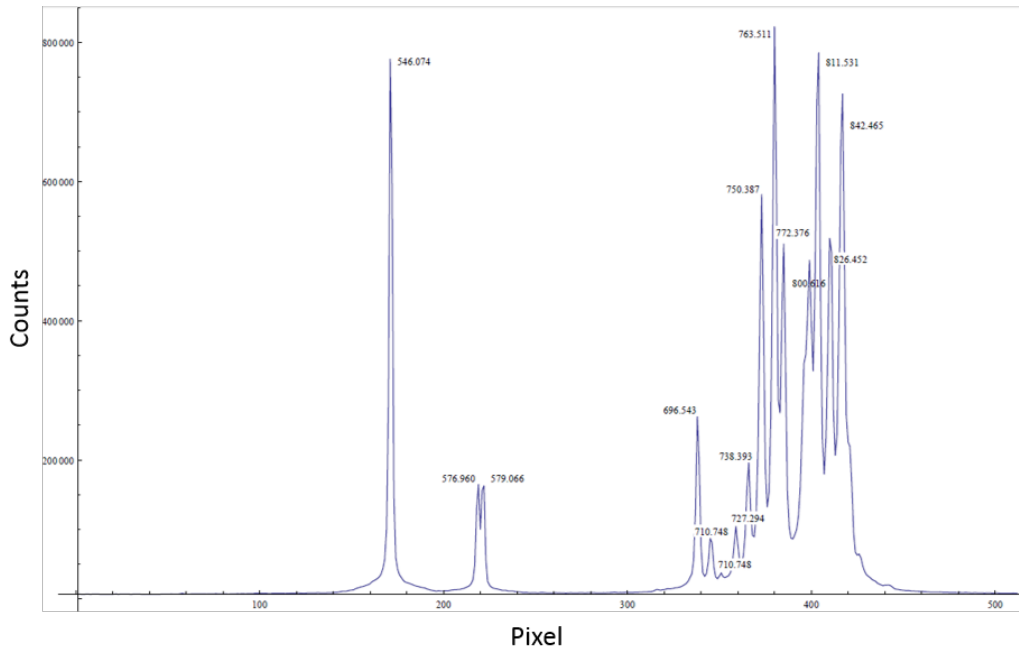
Figure 7.6: *Obtained spectrum from a calibration lamp using the set-up in figure 7.5. The wavelengths of the peaks are in nanometers.*

However the obtained spectrum is not calibrated. We need to determine which pixel corresponds to which wavelength. To translate pixels to wavelengths, the light of a calibration lamp is measured as shown in figure 7.6. The wavelengths of the visible peaks are known and coupled to athe corresponding pixels. To the obtained wavelength-pixel pairs a third order polynomial is fitted, resulting in the following translation from pixel to wavelength.

$$\lambda = 388.763 + 1.50565p - 0.00507764p^2 + 9.7635 * 10^{-6}p^3 \qquad (7.5)$$

where λ is the wavelength at pixel p.

Due to wavelength dependent transmittance of the spectroscopy set-up and wavelength dependent camera sensitivity, we also need to calibrate the set-up for light sensitivity. We need to convert counts captured by the camera to number of photons. Although we do not find an absolute scale for the number of photons, the calibration does allow us to compare the different peak heights. This calibration is done by measuring the spectrum of a 3200K black body and comparing it to its actual spectrum given by

$$P(\lambda, T) = \frac{2c}{\lambda^4} \frac{1}{\exp\left(\frac{hc}{\lambda k_B T}\right) - 1} \qquad (7.6)$$
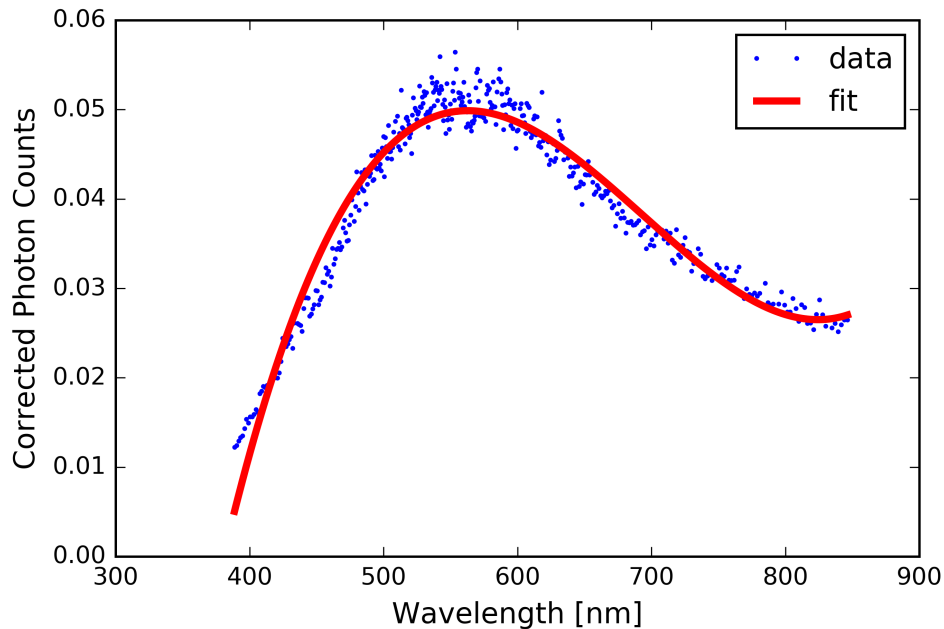
Figure 7.7: *Spectrum obtained before plasma is created (blue dots). The data is fitted to a third order polynomial (red line).*

where P is the photon-density at a certain wavelength, so $Pd\lambda$ is the number of photons emitted with wavelengths between λ and $\lambda + d\lambda$. h is Planck's constant and c light speed. Other symbols are as introduced before.

For each wavelength the experimentally obtained data is multiplied by the ratio of the theoretical photon density to the experimentally measured Planck curve.

After these calibrations a certain dark count spectrum remains. Two sequences, one with 10ns exposures and no gain, and another with 100ns exposures and 50/255 gain show the same background spectrum of the same intensity. However, they both defer from the measurements done for calibration where multiple exposures where digitally accumulated. This difference might cause the calibration to deform the dark counts to the observed data as seen in figure 7.7.

To adjust for this the spectrum is measured at a time no plasma is visible. The result of this is seen in figure 7.7. Note that the unit on the vertical axis is number of photons times a certain unknown factor. The spectrum is fitted to a third order polynomial given by the red line. This polynomial is then subtracted from all subsequent spectra.
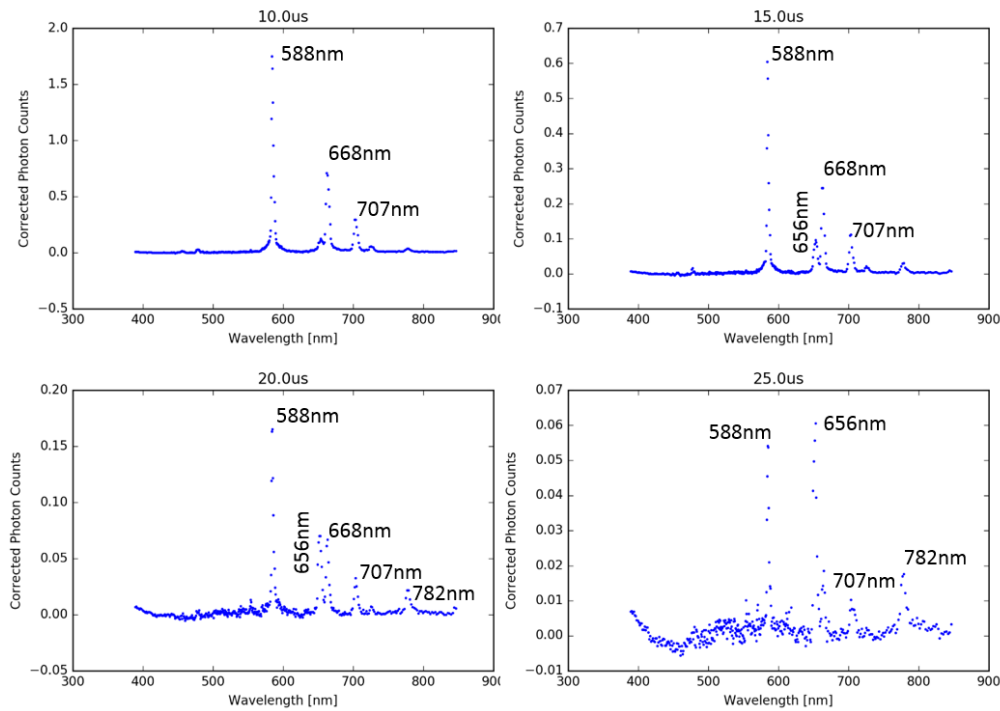
Figure 7.8: *Spectra of the light emitted by the plasma at delay times of 10, 15, 20 and 25 microseconds after ionization, measured by the set-up as seen in figure 7.5. The spectrum has been calibrated as described in the previous section. The major peaks have been labeled by the wavelength of their corresponding spectral line.*

Note that the spectrum is obtained from 389nm to 846nm. Wavelengths below 389nm were not captured because of the positioning of the camera, with 389nm being captured by the left most pixel. The camera sensitivity starts drops around 850nm. The low sensitivity causes the calibration process to yield noisy and untrustworthy results in this wavelength regime. Only 420 pixels have been used instead of the full sensor width of 512.

7.3.2   Results

Figure 7.8 shows the obtained spectra. The major peaks have been labeled by the wavelength of their corresponding spectral line. When determining the central wavelengths of these peaks from the data all peaks appear to have shifted four to five nanometers to the blue. This indicates that our calibration is slightly off.

Interesting is the peak at 656nm. While the other peaks drop in height
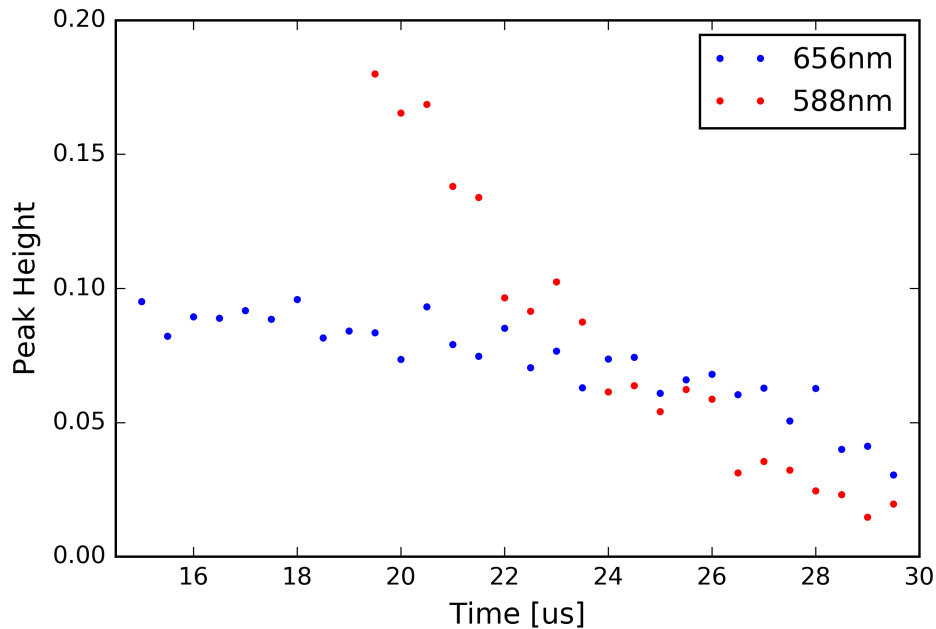
Figure 7.9: *Peak heights of the 656nm(blue) and 588nm(red) spectral lines extracted from the spectra as in figure 7.8, for each 0.5 microseconds a spectrum is made and the peak height extracted.*

as time progresses, this peak stays relatively constant. There are no spectral lines of Helium around the observed wavelength, which means it corresponds to the 656nm line of singly ionized Helium (He+).

There are multiple transitions within He+ that contribute to this line. The upper states of these transitions are in the n=6 shell. This is a high energy shell, which is unlikely to be reached through thermal collisions. Also, no other He+ lines are seen which would be expected from thermal excitation. Another possibility to create excited He+ is by recombination of electrons and fully ionized Helium. Which would mean the height of the 656nm line gives an indication for the recombination rate.

Spectra have been obtained for multiple delay times, each separated by 0.5 microseconds. From 15 microseconds the 656nm peak can be clearly distinguished from the 668nm peak. For each time-step a Gaussian is fitted to the peak at 656nm, of which the amplitudes are shown in figure 7.9 by the blue dots.

The drop in peak height of the 656nm peak is notably smaller than that of other peaks. For comparison the peak height of the 588nm neutral Helium line is shown in figure 7.9 by the red dots.
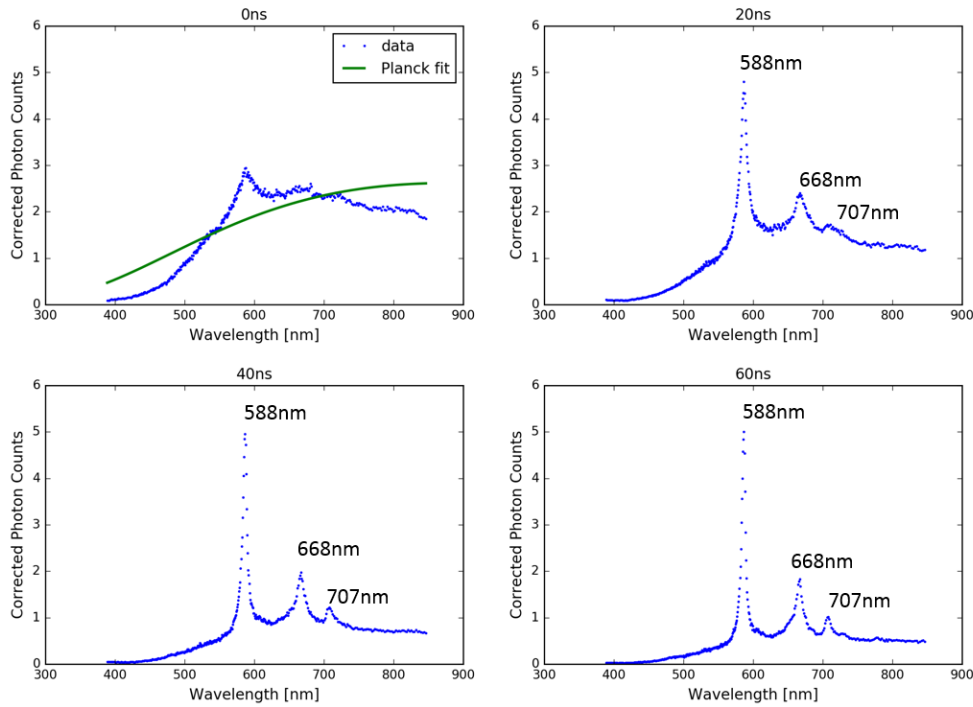
Figure 7.10: *Spectra of the light emitted by the plasma at delay times of 0,20,40 and 60 nanoseconds after ionization. The spectrum has been calibrated as described in the previous section. The major peak have been labeled by the wavelength of their corresponding spectral line. For the spectrum at 0ns a Planck curve has been fitted(green line).*

7.3.3 Ionization

The spectrum is also obtained around ionization. This spectrum is seen in figure 7.10. Note that the vertical axis is not compatible to that of figure 7.8, since different exposure setting were used.

For the spectrum taken at ionization (0ns) a Planck curve is fitted (green line). However, the fit is poor, indicating that the plasma does not radiate as a black body. This can be expected since black bodies are at thermal equilibrium, while the plasma is definitely not, after being created by an intense laser pulse.

As time progresses, the background radiation decreases and the neutral Helium spectral lines become the prominent source of light, confirming the results of the measurements done with filters as seen in figure 7.1.

Chapter 8

Conclusions

Videos   Several videos of the plasma are made which show the time-evolution of the light it emits. By looking from the back and side view a general idea can be formed of how the plasma evolves over time.

Ionization   We show that the two lobes visible at ionization are caused by the laser pulse beam geometry, which is mostly overlooked in literature. Using a model based on the beam geometry we predict the behavior of the two peaks and compare it to measurements. Although the model is fairly simple, we are able to effectively capture many of the observed phenomena. However, laser refocusing is needed to fully describe the behavior of the peaks when varying the pressure.

The ghost light, which is an image captured by the camera just before the actual plasma is visible, is proven to be an artifact of the camera.

Ring formation   We investigate the shock-waves expanding through the plasma and compare our plasma to a similar experiment and a simulation. From this the ring formation is explained through vortices created by opposing gas flows, one caused by the asymmetry of the two lobes and the other by the collapse of the second hot core. This explanations excludes linked magnetic field structures to be the cause of the ring formation.

Plasma shape   The shape of the cigar and ring stages of the plasma is determined for multiple pressures. Investigated are the diameter, hole diameter and the area of the images of the plasma. Lowering the pressure results in a smaller ring. However, lowering the pressure does not affect

53

to hole diameter significantly, indicating that the ring formation dynamics are independent of pressure.

Spectrum   The spectrum of the emitted light is obtained by using filters and by using a prism. It is shown that at ionization, a background radiation is found which differs from black-body radiation, indicating thermal equilibrium is not achieved. After ionization the light is predominantly created by transitions of neutral Helium. However, after 14 microseconds an increasing part of the light comes from a transition in He+, of which the excited states are hypothesized to be created from recombination of electrons with ionized Helium. Through Boltzmann analysis the temperature is derived, by which can be concluded no thermal equilibrium is reached before 10 microseconds.

Epilogue   It has been shown that the ring formation is caused solely by fluid dynamics, and no strong magnetic fields are found in the plasma. So the initial hope of finding linked magnetic structures is gone. But research on these plasma rings will continue at Leiden University, as Vincent Kooij is already working on inducing magnetic fields in the plasma rings. The results in this thesis describes many aspects of the plasma, providing useful information on the processes at play. With this information, we are yet one step closer to creating linked magnetic structures in the lab.

Bibliography

[1] Roel Burgwal. The effect of electric pre-ionization on the laser-induced breakdown of helium. 2015.

[2] Shankar Ghosh and Krishnan Mahesh. Numerical simulation of laser – induced breakdown in air. (January):1–22, 2008.

[3] Ch. Leela, Suman Bagchi, V. Rakesh Kumar, Surya P. Tewari, and P. Prem Kiran. Dynamics of laser induced micro-shock waves and hot core plasma in quiescent air. *Laser and Particle Beams*, 31(02):263–272, 2013.

[4] S K Monafred, W G Graham, T J Morgan, and L Hüwel. Spectroscopic characterization of laser-produced atmospheric pressure helium microplasmas. *Plasma Sources Science and Technology*, 20(4):049803–049803, 2011.

[5] P. Monot, T. Auguste, L. A. Lompré, G. Mainfray, and C. Manus. Focusing limits of a terawatt laser in an underdense plasma. *Journal of the Optical Society of America B*, 9(9):1579– 1584, 1992.

[6] C G Morgan. Laser-induced breakdown of gases. *Reports on Progress in Physics*, 38(5):621–665, 2001.

[7] NIST. http://physics.nist.gov/cgi-bin/ASD/lines1.pl.

[8] C. B. Smiet, S. Candelaresi, A. Thompson, J. Swearngin, J. W. Dalhuisen, and D. Bouwmeester. Self-Organizing Knotted Magnetic Structures in Plasma. *Physical Review Letters*, 115(9), 2015.